COBEM 2023 27TH INTERNATIONAL CONGRESS OF MECHANICAL ENGENEERING

ABCM Brazilian Society of Mechanical Sciences and Engineering
27th ABCM International Congress of Mechanical Engineering
December 04-08, 2023, Florianópolis-SC, Brazil

COB-2023-1793
A 3D CONSTITUTIVE MODEL FOR MODELLING MILLING INDUCED DAMAGE IN COMPOSITE LAMINATES

Sergio Luiz Moni Ribeiro Filho
Mauricio Vicente Donadon
Alfredo Rocha Faria
Technological Institute of Aeronauctics, Aeronautical and Aerospace division, IEA – Praça Marechal Eduardo Gomes, 50, Vila das Acácias, 12228-900, São José dos Campos
sergiomoni@ita.br, donadon@ita.br, arfaria@ita.br

Abstract. *Finite element models offer a cost-effective and innovative solution for virtually design machining strategies and predict failure modes in composite structures. This work introduces an energy-based formulation for a three-dimensional ply failure model to investigate the milling behaviour of UD carbon fibre laminate, using a VUMAT subroutine. This damage model integrates a continuum damage mechanics (CDM) with cohesive interface elements to predict both intra/translaminar and interlaminar failure modes. At the ply level, the CDM model takes in account in-plane shear failure, fibre failure (in tension/compression), and matrix cracking (in tension/compression). Machining-induced delamination is assessed using native cohesive interface elements, whose formulation is based on a bilinear traction-separation law, predicting the initiation and propagation of delaminations. Milling forces are predicted at each increment of time during the simulations. Experimental tests are conducted with two different cutting geometric tools under dry conditions to validate the model predictions. In general, a fairly good correlation between numerical predictions and experimental data in terms of milling force and damage patterns was found.*

Keywords: *Finite element, composite, milling*

1. INTRODUCTION

Polymers and composite materials constitute, nowadays, approximately 7.5% of the total mass of vehicles (Zhang et al., 2012). According to Hosseinzadeh et al. (2005), fibre-reinforced polymers have increasingly replaced steel in the automotive industry. As structural components, composites reinforced with glass (GFRP) and carbon fibres (CFRP) can reduce the vehicle weight by 20-35% and 40-60%, respectively (Das, 2001). This trend is also notably encouraging in aircraft industry where Boeing 757 recently used more than 57% by weight of FRCs to construct the mainframe structure (Cepero-Mejías et al., 2020), representing estimated savings of 15-20% of fuel relative to any other airplane structure (Singh et al., 2013).

The manufacturing of composite parts typically involves many machining operations, including drilling and milling, during the final processing before assembly (He et al., 2022). Consequently, strict dimensional tolerances and surface roughness are commonly required. However, the machining of abrasive fibers and tougher resin can subject the cutting tools to excessive stress concentration, leading to significant failure modes such as fiber pull-out, delamination, and matrix cracks. According to Cepero-Mejías et al. (2020), these machining-induced damages can adversely affect the surface quality of the machined component and serve as potential initiation points for failures when subjected to service loads. To comprehensively understand the mechanisms behind damage formation under different tool geometries and process variables, it is imperative to thoroughly study the initiation and progression of failures during composite machining (Wang et al., 2021). This requires conducting numerous machining trials to examine the impact of processing parameters on surface roughness and failure initiation during cutting. However, the high cost associated with composite materials and cutting tools imposes limitations on the extent and scope of experimental testing.

Finite element (FE) models offer a cost-effective and compelling alternative for virtually designing machining strategies, enabling the prediction of failure modes in composite structures and reducing test campaign costs (Cepero-Mejías et al., 2020; He et al., 2022, Wang et al., 2021). Two common types of damage modelling strategies found in machining FE models are energy-based and ply discount approach based models. Both strategies involve the development of macro and micro-scale models to reduce stiffness matrix parameters (Cepero-Mejías et al., 2020). Soldani et al. (2011) stated that the damage is the most sensible factor in FE modelling of composite cutting. The distribution of damage undergoes significant changes not only due to mesh size, shape, and orientation but also as a result of variations in the energy required to cause elemental failure. Santiuste et al. (2010) concluded that matrix damage and chip formation heavily depend on the energy required to lead to elemental failure. This energy also characterizes the composite behavior (brittle/ductile) during machining. Cepero-Mejias et al. (2020) noted that the implementation of the continuum damage mechanics (CDM) approach in composite cutting models realistically predicts

the fracture behavior of the translaminar interface between the fiber and matrix. However, only a limited number of existing FE models have addressed this approach.

This work presents an energy-based formulation for a tree-dimensional ply failure model to investigate the milling process behaviour of UD carbon fibre laminate. The proposed model combines continuum damage mechanics and stress-based fracture mechanics approaches within a unified context, enabling the analyse of the damage initiation and damage propagation. The constitutive model was implemented into ABAQUS/Explicit using VUMAT subroutine. The proposed formulation was verified against experimental data in terms of cutting force provided by the piezoelectric dynamometer and sub-surface damage identification with aid of an image acquisition system.

2. MATERIALS AND METHODS

2.1 Experimental setup

Milling tests were performed on a 5-axis vertical machining center (model DCM560) equipped with a Siemens-840D CNC control system. Solid carbide end mills with 1P222-XA (4 flutes) and 2P50-OA (7 flutes) codes, both with 6 mm diameter, were used. The cutting tools were chosen based on two different geometries, being the first typically used when milling non-ferrous materials (Fig. 1a) and the second are commonly used for non-metallic materials such as polymers and composites (Fig. 1b).

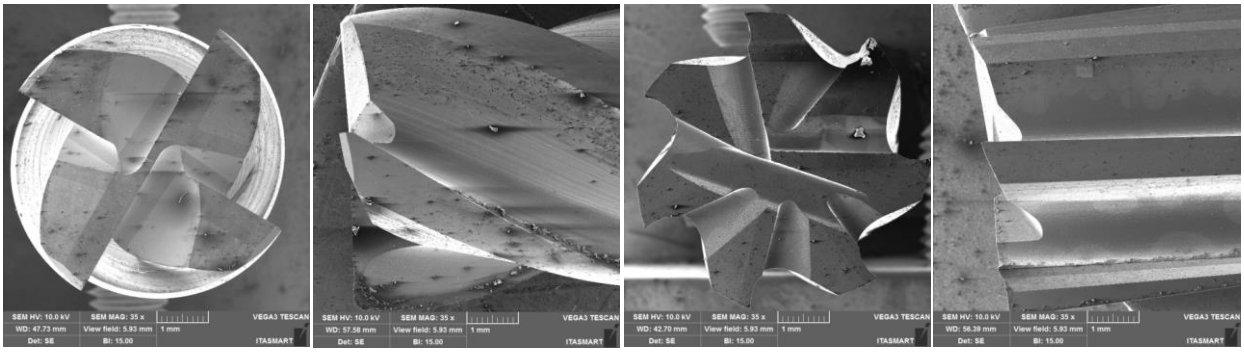

(a) (a') (b) (b')

Figure 1. Solid carbide end mill (a-a') 1P222-XA and (b-b') 2P50-OA.

The cutting forces were acquired by a 9265B 4-component Kistler dynamometer. The piezoelectric system was connected to a Kistler amplifier 5070, and the sensitivity was evaluated (pC/N) with a loss pass filter and an error curve determined in the range from 0 to 150 N. For accurate measurement of three orthogonal forces (Figure 2), the composite specimen was securely fixed to the piezoelectric dynamometer (Figure 3). In-plane images were captured to analyze the machining induced damage, while through-the-thickness images were taken to examine the progression of failure. The image acquisition system was composed of a high-speed CCD camera, Photron FASTCAM SA-Z. The camera was set to a frame rate of 30,000 frames per second (fps), enabling image acquisition at intervals of approximately 0.033 ms (corresponding to the cutting tool traveling approximately 66.7 mm). The exposure time was set at 1/400,000s to ensure optimal image quality. To achieve a high magnification of the burr formation zone, a Mitutoyo objective with 10x magnification and extended lens tubes was attached to the camera. This configuration provided an observation area of 1.84 x 1.23 mm². The acquired images had a resolution of 896 x 368 square pixels with an 8-bit dynamic range (256 gray levels) and a pixel calibration of 1.792 mm/pixel.

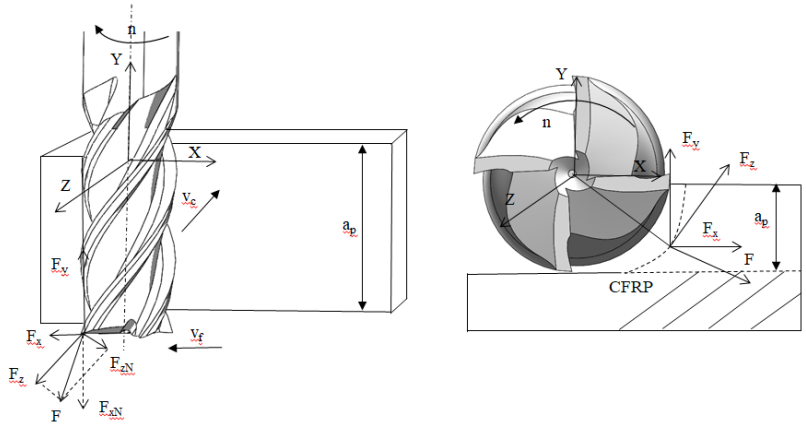

Figure 2. Schematics of milling forces experimentally measured.

Figure 3 shows the schematic milling setup. The cutting speed was determined based on the recommendation of the tool supplier and set to its maximum speed of 130 m/min. This value was chosen to maintain consistency with typical cutting speeds (80-120 m/min) since a lower speed would not intensify either the damage or cutting forces. By setting the milling parameters to their maximum values, the machining process simultaneously generates diverse damage and cutting forces. The depth of cut (0.4 mm) and feed rate (0.02 mm/t) was based on the geometry of the composite plates. These plates, supplied by Embraer, consisted of UD tape-based laminate of AS4/8552 UD carbon/epoxy layers and $[0^o]_{16}$ lay-up and had dimensions of 76.9 mm in length, 20 mm in width, and a thickness of 3.04 mm. The experiments were performed in dry condition and the factors cutting speed (130 mm/min), depth of cut (0.4 mm) and feed rate (mm/t) are kept constant.

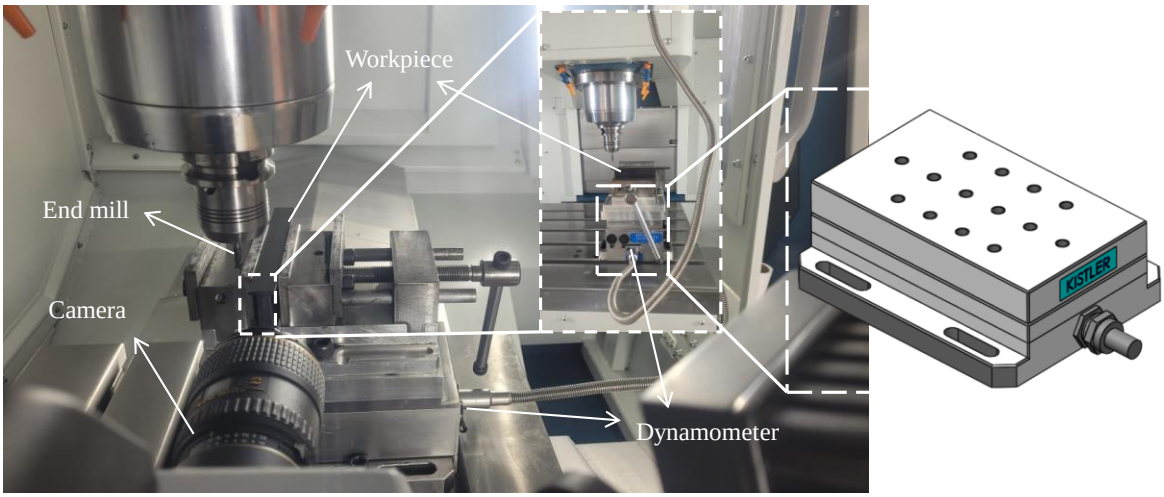

Figure 3. Schematic milling setup

2.2 Constitutive models

2.2.1 Intralaminar damage model

The intralaminar model formulation combines four modeling approaches, as proposed by Donadon et al. (2009). These approaches include failure criteria, fracture mechanics, plasticity, and damage mechanics. The aim is to accurately predict the five common failure modes observed in unidirectional (UD) composite materials: fiber failure in tension and compression, matrix cracking in tension and compression, and in-plane shear failure. To address fiber failure in compression, a formulation for fiber kinking was introduced, based on the work of Dávila and Camanho (2003) and Oliveira and Donadon (2020). This formulation takes into account the initial misalignment of fibers as a precursor to failure. Fiber kinking induces shearing stresses between the rotating fibers, leading to an increase in shearing stress levels and the onset of instability. Shapery (1995) has considered that the failure of misaligned fibers is closely linked to the formation of kink bands when localized matrix cracking occurs. Additionally, Garland et al. (2001) have assumed that other failure mechanisms, such as delamination and crushing, which can occur during uniaxial compression, are primarily triggered by matrix failure. In this context, this model approach accounts for stress computation within the kink band and enables evaluation of matrix failure modes inside the kinking band, both in tension and compression. The degradation in these modes is computed using strains on the matrix fracture plane, with a dedicated damage parameter. Furthermore, the well-known Puck and Schürmann (2004) failure criteria is implemented to assess matrix failure under tensile stress within the proposed model.

The proposed kink band formation in this study builds upon the formulation by Dávila and Camanho (2003). This failure criteria serves as a starting point to determine the orientation of the kink failure angle within a representative volume element (RVE). The rotation angle at which the fiber initiates the failure process under compressive conditions is determined by Equation 1.

$$k_{fail} = \arctan\left(\frac{1-\sqrt{1-4\left(\frac{S_{12}}{S_{11c}}+P_{tbc}\right)\frac{S_{12}}{S_{11c}}}}{2\left(\frac{S_{12}}{S_{11c}}+P_{tbc}\right)}\right) \quad (1)$$

The parameters $S_{11c,}$ S_{12}, and P_{tbc} represent the compressive strength of the fibre, in-plane shear strength, and the Puck and Schürmann failure index parameter for the material, respectively. Once the kink angle orientation, k_{fail}, is determined, the stress and strain tensors of the RVE (Oliveira and Donadon, 2020) are transformed into the proposed kink band formation, based on the methodology outlined by Davila and Camanho (2003) and, using the relevant

relations $[\sigma^k] = [T^k][\sigma][T^k]^T$and $[\varepsilon^k] = [T^k][\varepsilon][T^k]^T$, respectively. Details on the formulation for the equivalent strains that govern the material law for matrix failure in compression/tension and the computation of the damage parameter for fibre in compression within the kink band can be found in Oliveira and Donadon (2020).

A stress-based criteria was used to detect the damage initiation for fibre failure in tension, for matrix failure in tension, and for in-plane shear failure. The fracture and damage mechanics was combined within a unified context by using the smeared cracking approach, which relates the specific energy within a Representative Volume Element (RVE) with the fracture energy of the material for each particular failure mode. The non-linearity originated from the micro-cracks and the in-plane shear behaviour were modelled by using a plasticity approach. Damage evolution laws are stablished on hermitian cubic softening law employed to degrade the local stresses and avoid numerical instability. Table 1 shows the failure criteria to detect the damage onset at ply level.

Table 1. Failure criteria for damage onset detection.

Failure mode	Failure criteria	
Fibre in tension	$F_1^t(\sigma_1) = \frac{\sigma_1}{S_{11t}} \geq 1.0$	(2)
Matrix in tension	$F_2^t(\sigma_{nn}, \tau_{nl}, \tau_{nt}) = \left(\frac{\sigma_{nm}}{S_{22t}}\right)^2 + \left(\frac{\tau_{nl}}{S_{23}}\right)^2 + \left(\frac{\tau_{nt}}{S_{12}}\right)^2 \geq 1.0$	(3)
In-plane shear	$F_{12}(\tau_{12}) = \frac{\lvert\tau_{12}\rvert}{S_{12}} \geq 1.0$	(4)

The parameters S_{11t}, S_{11c}, S_{22t}, S_{22c}, S_{23}, S_{12} are the tensile strength and compressive strength in the fibre direction, the tensile and compressive strength in the matrix direction, out-of-plane shear strength and the in-plane shear strength, respectively. And the stresses σ_1, σ_2, τ_{23}, τ_{12} are the stresses applied in the fibre and matrix direction, and the out-of-plane and in-plane shear stresses, respectively. The friction coefficients μ_{nt} and μ_{nl}, the stresses σ_{nn}, τ_{nl}, τ_{nt} and the out-of-plane shear strength S_{23}^A are the Puck and Schurmann (2004) failure criteria parameters.

2.2.2 Interlaminar damage model

Interlaminar damage was modelled by using native interface elements available in ABAQUS. The local interfacial elastic stress-strain relationship is given as follows:

$$\begin{Bmatrix} t_n \\ t_s \\ t_t \end{Bmatrix} = \begin{bmatrix} E_{nn} & 0 & 0 \\ 0 & E_{ss} & 0 \\ 0 & 0 & E_{tt} \end{bmatrix} \begin{Bmatrix} \varepsilon_n \\ \varepsilon_s \\ \varepsilon_t \end{Bmatrix} \tag{5}$$

E_{nn}, E_{ss} and E_{tt} are the interface elastic properties components of the material in the cohesive zone between two adjacent plies and ε_n, ε_s e ε_t are the interfacial normal, and shear strains associated with mode I, mode II and mode III delamination.The model incorporated cohesive interface elements that facilitated a general contact formulation and propagation of failure between adjacent plies. By employing a traction-separation law, the contact formulation and cohesive zone model enabled the prediction of failure initiation and evolution of damage, where damage onset is predicted by using a stress-based quadratic formulation according to Equation 6.

$$\left\{\frac{\langle t_n \rangle}{t_n^0}\right\}^2 + \left(\frac{\langle t_s \rangle}{t_s^0}\right)^2 + \left(\frac{\langle t_t \rangle}{t_t^0}\right)^2 \geq 1.0 \tag{6}$$

The traction-separation formulation assumes initially linear elastic behavior, considering separation stresses t_n (normal direction), t_s (13 direction) and t_t (23 direction) associated with mode I delamination, followed by shear stress in the first direction related to mode II delamination and shear stress in the second direction associated with mode III delamination.

The proposed in-built model relies on a single damage parameter, D_{coh}, for tracking the progression of damage. This parameter is determined by equation 7, which takes into account δ_m^0, δ_m^f, and δ_m^{max}. Here, δ_m^0 represents the failure onset displacement, δ_m^f denotes the final displacement, and δ_m^{max} corresponds to the maximum displacement in the time history for the bi-linear softening law.

$$D_{coh} = \frac{\delta_m^f(\delta_m^{max} - \delta_m^0)}{\delta_m^{max}\left(\delta_m^f - \delta_m^0\right)} \tag{7}$$

The interface damage model formulation incorporates the Benzeggagh and Kenane criterion (1996), given in Equation 8, to address the propagation of mixed mode interlaminar failures based on energy criteria. The critical energy release rates or fracture toughness values associated with mode I delamination in the normal direction (G_{cn}), mode II delamination in the first shear direction (G_{sc}), and mode III delamination in the second shear direction (G_{ct}) were

utilized. The η parameter in the B-K formulation (1996) was assigned a value of 1.45, following the approach introduced by He et al. (2022).

$$G^C = G_\eta^C + \left(G_S^C - G_\eta^C\right)\left\{\frac{G_S}{G_T}\right\}^\eta \tag{8}$$

The interlaminar strain energy release rates were defined as G_n, G_s, and G_t for the normal direction (mode I delamination), first shear direction (mode II delamination), and second shear direction (mode III delamination), respectively. The total strain energy release rate (G_T) was calculated as the sum of G_n, G_s, and G_t, while the shear strain energy release rate (G_S) was obtained by combining G_s and G_t.

2.3 Finite element modelling

The milling process was modelled considering a dynamic non-linear finite element using an explicit time integration scheme. A brick element C3D8R, available in ABAQUS Explicit, was used to model the UD composite carbon/epoxy. The mesh size applied was 0.10 mm per 0.10 mm in the cutting region and 0.6 mm per 0.3 in the clamp region. The specimens have a total of 16 plies, where each ply has 0.19 mm in thickness and 76.9 mm in length, the total thickness is 3.04 mm. The tool was modelled considering an isothermal rigid body. The miller cutter was modelled based on the tools code 1P222 and 2P50 produced by SANDVIK Coromant™ with 6 mm of diameter. The displacement of the tool was considered only in the cutting direction. The rotation and the linear movement of the tool were constrained at the reference point (RP). The cutting speed (130 m/min) was implemented at the RP in the cutting direction. The material interlaminar strength, elastic and fracture properties were extracted from HexPly 8552 data sheet from the carbon fibre plies manufacturer Hexcel and characterised in the Laboratory of New Concepts in Aeronautics (LNCA). Two contact approaches were applied for the milling model: contact between the composite structure and analytic rigid surface (cutting tool) and contact between adjacent plies. Figure 4 shows the FE schematic model.

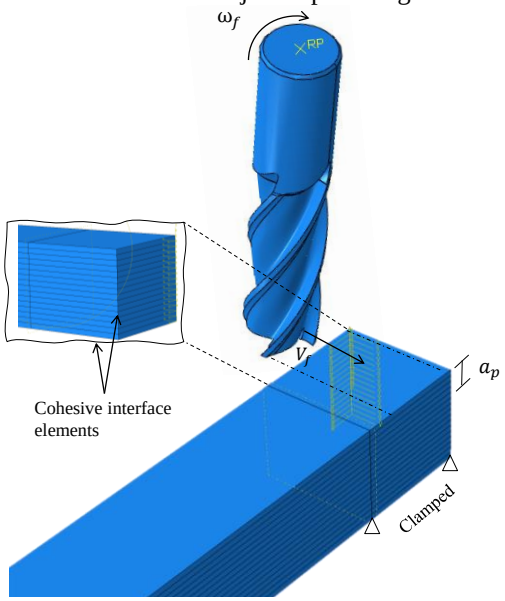

Figure 4. Schematic FE model

2.3.1 Interaction between UD laminate structure and cutting tool

General contact formulation available in ABAQUS/Explicit was combined with a “refinement” through contact pairs to enhance the accuracy and effectiveness of the model by ensuring that there was no interpenetration or overlap between the UD carbon fibre laminate and cutting tool surfaces. By utilizing contact pairs, interaction surfaces were created within the parts, and the contact pair formulation carefully monitored the geometry, position, and size of these selected surfaces that might come into contact. The first surface corresponds to the analytic rigid cutting tool, while the second encompasses all exterior and interior element surfaces in the composite structure. This was made possible by utilizing the "all-inclusive" contact surface formulation available in ABAQUS/Explicit, which proved highly beneficial in this particular model. In this approach, the algorithm was capable of accessing the internal surfaces of the mesh within the composite structure. As the elements were cut by the analytic rigid surface, the general contact algorithm tracked the internal surfaces of the adjacent elements. In the event that an element was deleted from the simulation, the

internal surface of the neighboring elements, which was initially not in contact with the rigid tool, assumed contact. This behavior was due to the effective tracking of internal surfaces by the general contact algorithm.

The friction coefficient μ played a crucial role in the cutting phenomenon, influencing morphology, force, and energy-displacement response (Liang, et al., 2022). To accurately model the energy absorption, a static-kinetic exponential decay law was applied using Equation 9 (Figure 5). The static coefficient μ_s was set at 0.2 for zero slip rate, the kinetic coefficient μ_k at 0.1 for a slip rate of 50, and the kinetic friction coefficient at 0.05 for an "infinity" slip rate ($\dot{\gamma}_{eq}$) in the ABAQUS/Explicit formulation. The variation in friction coefficients was informed by the lubrificant role of debris in the milling phenomenon, as studied by Sheikh-Ahmad et al. (2021). This comprehensive approach allowed for a more accurate representation of the milling behavior and its associated effects on force, energy, and deformation during the simulation. F_f

$$\mu = \mu_k + (\mu_s - \mu_k)e^{-d_c\dot{\gamma}_{eq}} \tag{9}$$

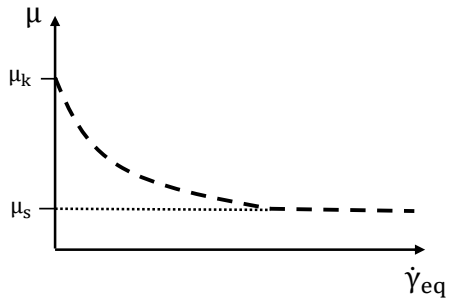

Figure 5. Friction coefficient decay lay as function of the slip rate $\dot{\gamma}_{eq}$

2.3.2 Interaction between adjacent plies

In terms of the interaction between adjacent plies, which represents the resin (epoxy polymer) area between layers, a cohesive contact formulation was implemented. Similar to the contact between the UD laminate and the cutting tool, a formulation "hard" was applied for normal contact, while a "friction" formulation was utilized for tangential contact. Here, is important to note that the interlaminar mechanical properties and strengths (Table 2) were incorporated into the model as input parameters. Additionally, the friction coefficient between fibre to fibre plays a significant role in this context, as highlighted by Yoon and Kang (2023). Therefore, a friction coefficient value of 0.28 was assigned to the contact between adjacent plies.

Table 2. Interface mechanical properties.

Mechanical properties	Parameter	Value
Interlaminar fracture toughness[a]	G_{Ic}	0.1977 kJ/m²
	$G_{IIc} = G_{IIIc}$	1.0098 kJ/m²
Strenght properties[b]	$t_n = t_s = t_t$	124 MPa
	η	1.45[d]
Elastic properties[c]	E_{nn}	2.97 GPa
	$E_{ss} = E_{tt}$	1.08 GPa
Intralaminar fracture toughness	$G_{1_f}^{t}$ [d]	133 kJ/m²
	$G_{1_f}^{c}$ [d]	40 kJ/m²
	$G_{2_m}^{t}$ [e]	0.1977 kJ/m²
	$G_{2_m}^{c} = G_{shear}$ [f]	1.0098 kJ/m²

[a] Values extracted from Sales et al. (2016).
[b] Values extracted from Hexcel 8552 material data sheet.
[c] Values measured at LNCA.
[d] Values extracted from Tan et al. (2015).
[e] Values assumed to be equal to GIc, according to Czabaj and Ratcliffe (2013).
[f] Values assumed to be equal to GIIc, according to (Tan et al., 2015).

2.3.3 Element deletion

An element deletion criterion was implemented to mitigate the effects related to element distortion. This approach involves examining the determinant of the gradient deformation of each element and comparing it against user-defined minimum and maximum values (Oliveria and Donadon, 2020). These values determine whether an element should be retained or removed from the simulation. The approach required the user to input two values, $|F|_{min}$ and $|F|_{max}$, which

established the acceptable range for the determinant of the deformation gradient, denoted as |F|. By comparing the calculated |F| with these user-defined thresholds, a decision was made regarding the inclusion or removal of elements in the simulation. Equation 10 expresses the relationship between the initial volume V_0 and the current volume V of an element at each time step during the simulation. In this particular study, $|F|_{min}$ was set to 0.90, while $|F|_{max}$ was set to 1.8. As a result, any elements with |F| values below 0.90 or above 1.8 were identified for removal from the simulation. This mechanism effectively addressed issues arising from element distortion, ensuring accurate and reliable results.

$$|F| = \frac{V}{V_0} \tag{10}$$

3. RESULTS AND DISCUSSION

Cutting forces are predicted at each increment of time during the feed of the cutter in the cutting direction. Given the different geometry of cutting tools and unidirectional CRFP anisotropic response, the predicted cutting force reveals similar behaviour to the experimental curve for both end mills. Figure 6 shows a significant increase of cutting force (Fz, see Figure 2) induced by end mill engagement (stage 1), oscillations of the cutting force because the end-mill crosses the matrix and fibre layers (stage 2), and a decrease of force upon the exit of the end mill (stage 3). In general, the average maximum cutting force in the experimental trial was 38.72 N and 44.64 N for a seven (2P50) and four flute end mill (1P222), whereas FE model estimated 39.8N and 47.31 N, respectively. This shows a fairly good correlation between numerical predictions and experimental data, with 5.98% and 2.79% deviation from the respective test results. The slight variation can be attributed to the changes in the contact condition within ABAQUS/Explicit, as well as the element criterion used to remove damaged elements.

As shown in Figure 6, the difference between the forces arising the variation in cutting tool geometric conditions is also noted. The increase in cutting force level indicates the rise effect of the end mill flute in chip formation during milling. The oscillations of the force signal can be described by the rise of the plastic deformation and the material heterogeneous response during the chip formation. This implies that the higher force level of the 1P222 tool resulted in higher plastic deformation (Figure 10).

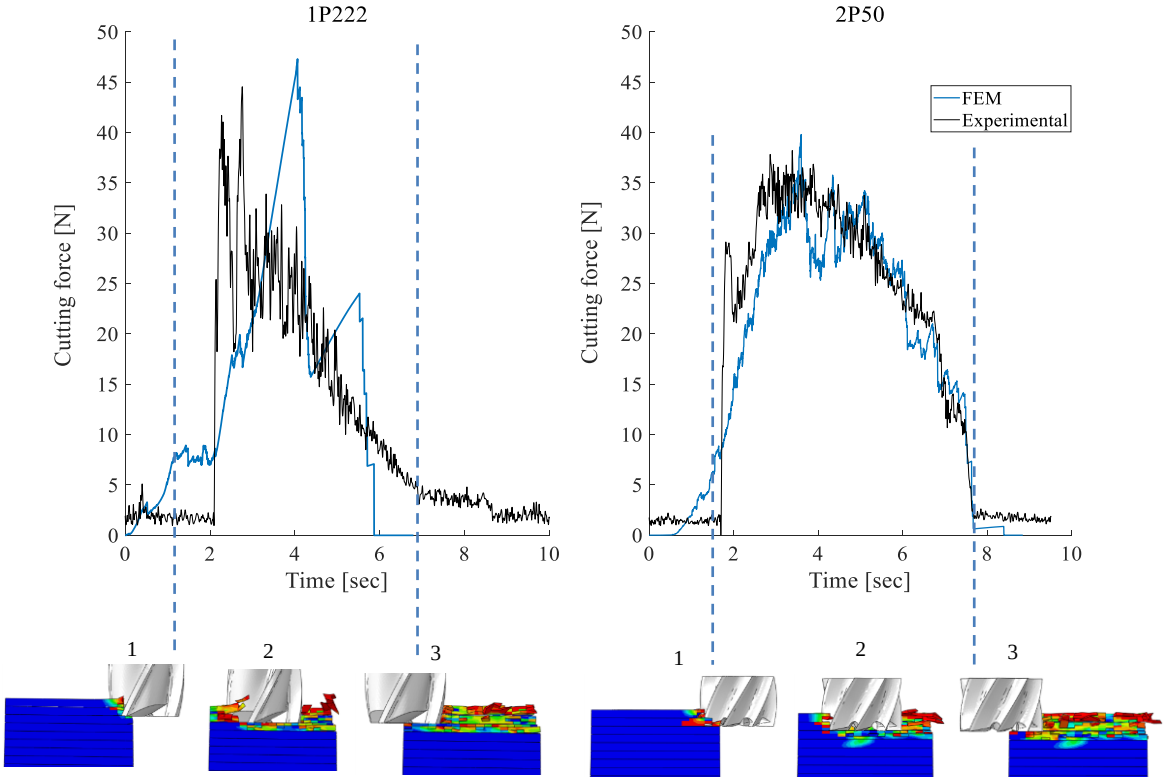

Figure 6. Comparison between experimental and numerical predictions force-time histories.

The five failure modes predicted by the proposed damage model are showed in Fig. 7. For each of the five failure mechanisms, the fibre damage and matrix crack failure are depicted by the red elements. According to the Puck and Schurmann failure criteria (2004), the matrix cracking in tension was dominant in the zone beneath the machine surface, followed by matrix crushing damage. These two damage mechanisms covered most of the machined surface because of the stress state of material during milling met the matrix failure initiation. The fibre crushing (compression) and in-plane shear failure were also significant, where the shear failure have a larger damage surface area than the fibre failure.

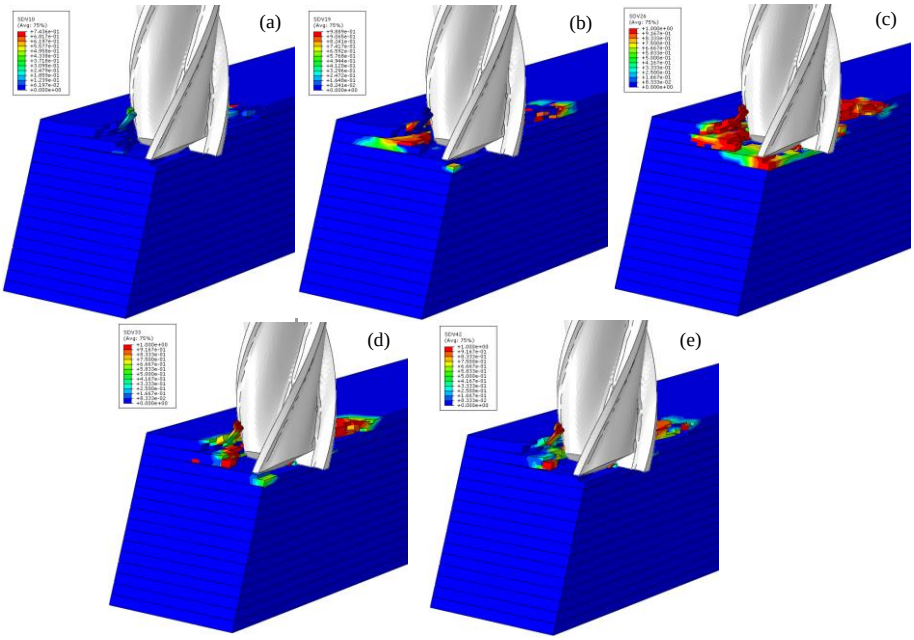

Figure 7. Damage parameters for milling process: (a) fibre in tension, (b) fibre in compression, (c) matrix in tension, (d) matrix in compression and (e) In-plane shear.

The images obtained by the image acquisition system during the milling process were correlated to the damage predicted by the FE model. Those images were selected to capture most of the chip formation and milling induced damage and do not correspond to the peak cutting force. The comparison in the initial tool flute entry and entire end-mill engagement are shown in Figure 8a and Figure 8b. As the tool advances in the workpiece, two mechanisms lead to the formation of chip: delamination and the combination of crushing (Fig. 7b, d) and shearing (Fig. 7e) of the fibres/matrix. Primarily, the compression of the laminate under the tool edge takes place and then is torn by the tensile stresses (Fig. 7c). Once the interface has failed, shear stresses build up in the cutting tool. Failure propagates perpendicularly to the cutting direction due to the fibre-matrix debonding under the effect of shear stress. In this way, it is tenable to conclude that the cross section experimental images verify the predicted morphology and milling phenomenon. In general, the cohesive zone elements between the adjacent plies, in combination the VUMAT constitutive model, predicted the occurrence of the breakage, interplay delamination and burr formation with reasonable accuracy.

Figure 8a-b ilustrates the relationship between the number of flutes to the milling induced damage. The geometries of 1P222 (4 flutes) and 2P50 (7 flutes) end mills are entirely different in the exit surface. End mills with a higher number of flutes exhibit a larger core and smaller flute valleys in comparison to tools with fewer flutes. This can imply in a reduced flute depth, which restricts the available space for chip accumulation. As result, the chips are smaller and more fragmented, reducing the plastic deformation and enhancing the surface finish. According Joshi and Bolar (2021), an increase in the number of flutes leads to a decrease in chip load, thereby minimizing the milling force and improving surface roughness.

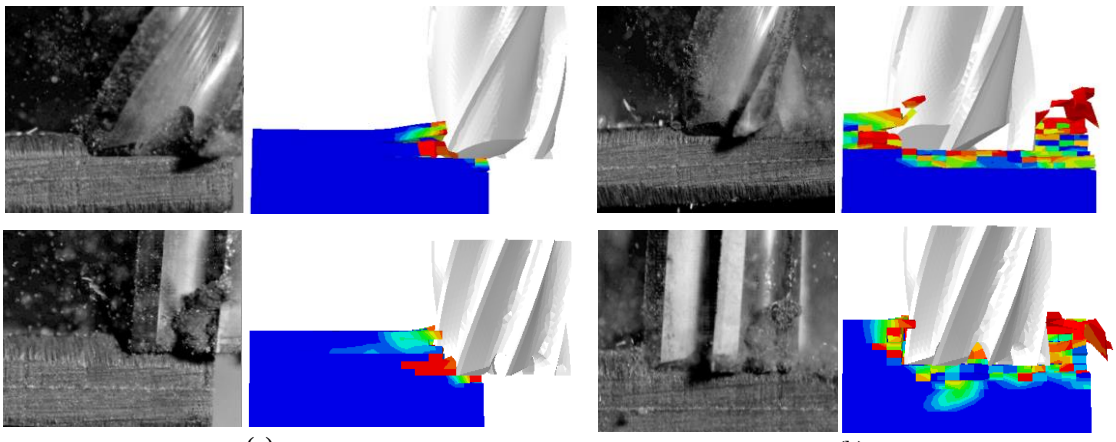

(a) (b)

Figure 9. Comparison between experimental and numerical predictions (a) initial tool flute entry and (b) entire end-mill engagement.

4. CONCLUSIONS

A 3D constitutive methodology for modelling composite structures under the milling process has been presented and discussed in this paper. The following contributions can be drawn:

- The proposed formulation enables the prediction of failure modes in composites under milling process within an energy based framework, accounting for kink band formation, for fibre failure/matrix in tension/compression and for in-plane shear failure;
- The cutting force predictions were in good agreement with the experimental results, with 5.98% and 2.79% deviation from the respective 1P222 and 2P50 end mills;
- The number of end mill flutes decreases the cutting force of the composite structures and, consequently, the milling induced damage;
- The matrix cracking was the most significant damage in the zone beneath the machine surface. The cohesive zone elements between the adjacent plies, in combination the VUMAT constitutive model, accurately predicted fibre failure mode, matrix cracking characteristics and interlaminar failures;
- The FE model predicted most of the damage features observed experimentally including chip formation and interplay delamination with good accuracy;
- The present study was focused on the effect of different geometries of end mill. Further studies will consider the subsequent variation of the cutting strategies.

5. ACKNOWLEDGEMENTS

The authors would like to thank the Capes schorlarchip, CNPq (Grant No. 301069/2019-0) and Sandvik Coromant Company for kindly provided the tools.

6. REFERENCES

Benzeggagh, M.L., Kenane, M. 1996. “Measurement of mixed-mode delamination fracture toughness of unidirectional glass/epoxy composites with mixed-mode bending apparatus”. Compos Science Technology. V. 56(4), p. 439–449.

Cepero-Mejías, F., Curiel-Sosa, J.L., Blázquez, A., Yu, T.T., Kerrigan, K., Phadnis, V.A. 2020. “Review of recent developments and induced damage assessment in the modelling of the machining of long fibre reinforced polymer composites”. *Composite Structures*, v. 240, p. 112006.

Czabaj, M.W., Ratcliffe, J.G. 2013. “Comparison of intralaminar and interlaminar mode I fracture toughnesses of a unidirectional IM7/8552 carbon/epoxy composite”. *Composite Science Technology*, v. 89, p. 15–23.

Das S. 2001. “The cost of automotive polymer composites: a review and assessment of DOE‟s lightweight materials composites research”. Oak Ridge National Laboratory, p. 1.

Davila, C.G., Camanho, P.P. 2003. “Failure criteria for FRP laminates in plane stress. USA: National Aeronautics and Space Administration”. Technical Report. NASA/TM-2003-212663.

Donadon, M.V., Almeida, S.F.M., Arbelo, M.A., Faria, A.R. 2009. “A three-dimensional ply failure model for composite structures”. *International Journal Aerospace Engineering*, https://doi.org/10.1155/2009/486063.

Garland, B.D, Beyerlein, I.J., Schadler, L. 2001. “The development of compression damage zones in fibrous composites”. *Composites Science and Technology*, v. 61(16), pp. 2461–2480, doi:10.1016/s0266-3538(01)00176-2.

He, Y., Wan, Li, L., Wan, M., Xue, H. 2022. “Three-dimension of milling carbon/epoxy composites”. *Composite Structures*, v. 282, p. 115037

Hosseinzadeh, R., Shokrieh, M.M., Lessard, L.B. 2005. “Parametric study of automotive composite bumper beams subjected to low-velocity impacts”. *Composite Structures*, v. 68, p. 419–27.

Joshi, S.N. and Bolar, G. “Influence of end mill geometry on milling force and surface integrity while machining low rigidity parts”. *Journal of the Institution of Engineers (India): Series C*, v. 102, p. 1503-1511.

Liang, X., Liu, Z., Wang, B., Wang, C., Cheung, C.F. 2022. “Friction behaviors in the metal cutting process: state of the art and future perspectives”. *International Journal of Extreme Manufacturing*, v. 5, p. 012002.

Oliveira, S.A.C., and Donadon, M.V. 2020. “A 3D progressive failure model for crushing simulations in composite structures”. International Journal of Crashworthiness”. *International Journal of Crashworthiness*, v. 27, p. 591-693.

Puck A, Schurmann H. 2004. “Failure analysis of FRP laminates by € means of physically based phenomenological models. In: Failure criteria in fibre reinforced polymer composites”. Chapter 3.7; p. 832–876

Sales, R.C.M., Endo, B.L.R.D., Donadon, M.V. 2016. “Influence of temperature on interlaminar fracture toughness of a carbon fibre-epoxy composite material”. *Advanced Materials Research*, v. 2016, p. 1135–51.

Santiuste, C., Soldani, X., Miguélez, M.H. 2010. “Machining FEM model of long fiber composites for aeronautical components”. *Composite Structures*, v. 92(3), p. 691–698.

Schapery, R.A., 1995. "Prediction of Compressive Strength and Kink Bands in Composites Using a Work Potential," *International Journal of Solids and Structures*, v. 32, No. 6-7, pp. 739-765.

Sheikh-Ahmad, J., Almaskari, F. & El-Hofy, M. 2021. "Characterization of the cutting forces and friction behavior in machining UD-CFRP using slot milling test". *Int J Adv Manuf Technol*, v. 112, p. 3471–3483, https://doi.org/10.1007/s00170-020-06544-8

Singh, A. P., Sharma, M., & Singh, I. 2013. "A review of modeling and control during drilling of fiber reinforced plastic composites". *Composites Part B: Engineering*, v. 47, p. 118–125.

Soldani, X., Santiuste, C., Muñoz-Sánchez, A., Miguélez, M.H. 2011. "Influence of tool geometry and numerical parameters when modeling orthogonal cutting of LFRP composites". *Composites Part A: Applied Science and Manufacturing*, v. 42(9), p. 1205–1216.

Tan, W., Falzon, B.G., Price, M. 2015. "Predicting the crushing behaviour of composite material using high-fidelity finite element modelling". *Int J Crashworthiness*. V. 20(1), p. 60–77.

Wang, X., Wang, F., Gu, T., Jia, Z., Shi, Yu. 2021. "Computational simulation of the damage response for machining long fibre reinforced plastic (LFRP) composite parts: A review". *Composites Part A: Applied Science and Manufacturing*, v. 143, p. 106296.

Yoon, M. and Kang, G-H. 2023. "Effect of dynamic friction and static friction in finite element analysis of carbon fiber preform". *Polymer composites*, v. 44(4), p. 2396-2404.

Zhang J, Chaisombat, K., He, S., Wang C.H. 2012. "Hybrid composite laminates reinforced with glass/carbon woven fabrics for lightweight load bearing structures". *Materials & Design*. v. 6, p. 75-80.

7. RESPONSIBILITY NOTICE

The authors are the only responsible for the printed material included in this paper.